Ultrafast phonon-driven charge transfer in van der Waals heterostructures

Received: 8 April 2022 | Revised: 14 June 2022 | Accepted: 20 June 2022

DOI: 10.1002/ntls.20220014

RESEARCH ARTICLE

Natural Sciences

Ultrafast phonon-driven charge transfer in van der Waals heterostructures

Giuseppe Meneghini[1] | **Samuel Brem**[1] | **Ermin Malic**[1,2]

[1]Department of Physics, Philipps University of Marburg, Marburg, Germany

[2]Department of Physics, Chalmers University of Technology, Göteborg, Sweden

Correspondence
Giuseppe Meneghini, Department of Physics, Philipps University of Marburg, 35037 Marburg, Germany.
Email: giuseppe.meneghini@physik.uni-marburg.de

Funding information
Graphene Flagship, Grant/Award Number: 881603; Deutsche Forschungsgemeinschaft, Grant/Award Number: SFB 1083 (Project B9)

Abstract

Van der Waals heterostructures built by vertically stacked transition metal dichalcogenides (TMDs) exhibit a rich energy landscape, including interlayer and intervalley excitons. Recent experiments demonstrated an ultrafast charge transfer in TMD heterostructures. However, the nature of the charge transfer process has remained elusive. Based on a microscopic and material-realistic exciton theory, we reveal that phonon-mediated scattering via strongly hybridized intervalley excitons governs the charge transfer process that occurs on a sub-100fs timescale. We track the time-, momentum-, and energy-resolved relaxation dynamics of optically excited excitons and determine the temperature- and stacking-dependent charge transfer time for different TMD bilayers. The provided insights present a major step in microscopic understanding of the technologically important charge transfer process in van der Waals heterostructures.

Key Points:

- Microscopic and fully quantum-mechanic model is developed to calculate exciton dynamics in van der Waals heterostructures
- Charge transfer occurs on a femtosecond timescale and is a phonon-mediated two-step process
- Strongly hybridized dark exciton states play a crucial role for the charge transfer

KEYWORDS
charge transfer dynamics, dark excitons, exciton dynamics, exciton hybridization, van der Waals heterostructures

Transition-metal dichalcogenides (TMDs) have been in the focus of current research due to their enhanced light-matter and Coulomb interaction leading to a rich energy landscape of tightly bound excitons.[1–4] Stacking TMD monolayers into van der Waals heterostructures introduces spatially separated interlayer states adding another exciton species with long lifetimes and an out-of-plane dipole moment.[5–14] Recent experiments demonstrated the ultrafast charge transfer in optically excited TMD heterobilayers resulting in a formation of interlayer states on a sub-picosecond timescale.[15–20] Typically, TMD heterobilayers exhibit a type-II band alignment[21,22] favoring the tunneling of an electron or hole into the opposite layer. However, the underlying microscopic nature of the charge transfer process has not yet been well understood. In an early previous work, we have suggested a defect-assisted interlayer tunneling directly at

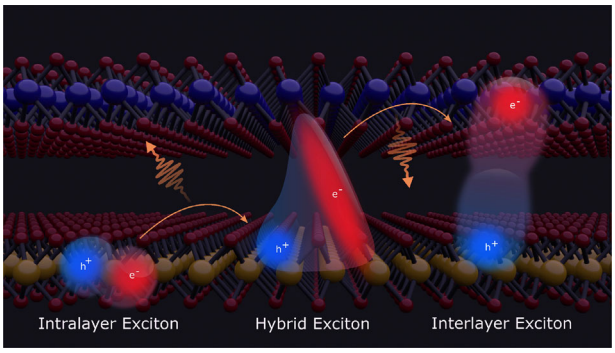

FIGURE 1 Sketch of the charge transfer process. Starting from an exciton localized in the bottom layer, phonon-mediated scattering to a hybrid exciton state (where, e.g., the electron lives in both layers) allows for the transfer of the charge (here electron) to the upper layer resulting in a spatially separated interlayer exciton state. In analogy, hole transfer can also take place if hybrid excitons with delocalized holes are present

the K point.[18,23] Alternatively, a phonon-mediated charge transfer could occur involving intervalley scattering to the strongly hybridized Λ or Γ valleys.[24–26] A sophisticated microscopic model of such a phonon-assisted formation of interlayer excitons is still missing.

In this work, we address this open question and reveal the crucial many-particle mechanism behind the ultrafast charge transfer in TMD heterostructures. To this end, we combine first-principle calculations[27] with the excitonic density matrix formalism[28,29] to obtain a material-realistic model of the excitonic energy landscape, the internal substructure of different exciton species, and the phonon-mediated scattering into layer-hybridized dark intervalley states.[30,31] We first calculate the exciton energy landscape of the exemplary MoS_2-WS_2 and $MoSe_2$-WSe_2 heterostructures by solving the Wannier equation for perfectly layer-polarized intra- and interlayer excitons and subsequently computing hybrid excitons based on first-principle interlayer tunneling parameters.[18,23,28,30,31] Then, we develop and numerically solve equations of motion describing the time- and momentum-resolved evolution of hybrid excitons. This allows us to track the relaxation dynamics of excitons from optically excited intralayer excitons toward charge separated interlayer exciton states. We identify the phonon-mediated intervalley scattering from intralayer KK into the strongly hybridized KΛ' excitons, followed by the relaxation into energetically lower interlayer $KK^{(\prime)}$ states, as the crucial mechanism behind the ultrafast charge transfer in these heterostructures, cf. Figure 1. We further determine the characteristic temperature- and stacking-dependent charge transfer time that can guide future experiments investigating interlayer excitons in van der Waals heterostructures.

Microscopic approach

The starting point of this work is the Hamilton operator describing electrons and holes of the heterostructure in the basis of monolayer eigenstates (localized in one of both layers). Here, we include a stacking-dependent alignment shift of the two monolayer band structures[32] as well as interlayer tunneling terms resulting from the wave function overlap between the adjacent layers. The necessary material-specific parameters have been extracted from first-principle calculations.[27] Moreover, we include many-particle interaction Hamiltonians, such as electron–light and electron–phonon coupling, as well as the Coulomb interaction between electrons and holes. Here, the scattering between electrons and photons/phonons preferably occurs locally within one of the two layers, whereas we explicitly include the Coulomb interaction between particles residing in different layers. The different intra- and interlayer Coulomb matrix elements are computed with a modified Keldysh-type potential[23,28,30] accounting for the dielectric environment created by the TMD layers and the substrate.[33] To achieve a numerically feasible model, we set the twist-angle between the two monolayers to zero and study the charge transfer in a spatially homogeneous system characterized by a single atomic alignment. Although the twist-angle is known to have a large impact on the hybridization of exciton states,[30] we expect the qualitative charge transfer behavior to remain the same also in twisted heterostructures. Moreover, we do not consider spin-flipping processes and restrict our model to the optically active (A exciton) spin configuration, as the spin-flipping processes are expected to occur on a slower timescale.[34,35]

Now, we derive the dynamics of the system by initially performing a series of basis transformations. First, we solve the Wannier equation for pure intra- or interlayer excitons[23] and use the eigenfuctions $\psi^{\mu}(\mathbf{k})$ to introduce a new set of excitonic operators[30] $X^{\mu\dagger}_{\mathbf{Q}} = \sum_{\mathbf{k}} \psi^{\mu}(\mathbf{k}) a^{\dagger}_{c,\zeta_e,L_e,\mathbf{k}+\alpha\mathbf{Q}} a_{v,\zeta_h,L_h,\mathbf{k}-\beta\mathbf{Q}}$ with the compound quantum number $\mu = (n, \zeta, L)$ labeling the excitonic states. Here, n is associated with the series of Rydberg-like states determining the relative electron-hole motion, $\zeta = (\zeta_e, \zeta_h)$ denotes the electron and hole valleys, and the layer compound index $L = (L_e, L_h)$ contains the electron and hole layer. Furthermore, we have introduced the center-of-mass momentum $\mathbf{Q}$ and the relative momentum $\mathbf{k}$ between electrons and holes. The operator $a_i^{(\dagger)}$ is annihilating (creating) electrons with the set of quantum numbers denoted by i. We use the new exciton operators to perform a basis transformation to obtain an effective single-particle Hamiltonian for excitons, reading

$$H_X = \sum_{\mu\mathbf{Q}} E^{\mu}_{\mathbf{Q}} X^{\mu\dagger}_{\mathbf{Q}} X^{\mu}_{\mathbf{Q}} + \sum_{\mu\nu\mathbf{Q}} \mathcal{T}_{\mu\nu} X^{\mu\dagger}_{\mathbf{Q}} X^{\nu}_{\mathbf{Q}} \tag{1}$$

with the exciton energy $E^{\mu}_{\mathbf{Q}}$ obtained from the Wannier equation and the excitonic tunneling matrix elements $\mathcal{T}_{\mu\nu}$, which contain apart from electronic tunneling rates also the overlap of excitonic wave functions.

Next, we diagonalize the exciton Hamiltonian Equation (1) by introducing a new set of operators $Y^{\eta}_{\mathbf{Q}} = \sum_{\mu} c^{\eta}_{\mu}(\mathbf{Q}) X^{\mu}_{\mathbf{Q}}$ describing hybrid excitons. These are layer-hybridized states consisting of intra- and interlayer excitons with the mixing coefficients $c^{\eta}_{\mu}(\mathbf{Q})$ and the new quantum number η defining the hybrid-exciton bands. The diagonalized Hamiltonian reads in this basis $H_Y = \sum_{\eta} \mathcal{E}^{\eta}_{\mathbf{Q}} Y^{\eta\dagger}_{\mathbf{Q}} Y^{\eta}_{\mathbf{Q}}$ with

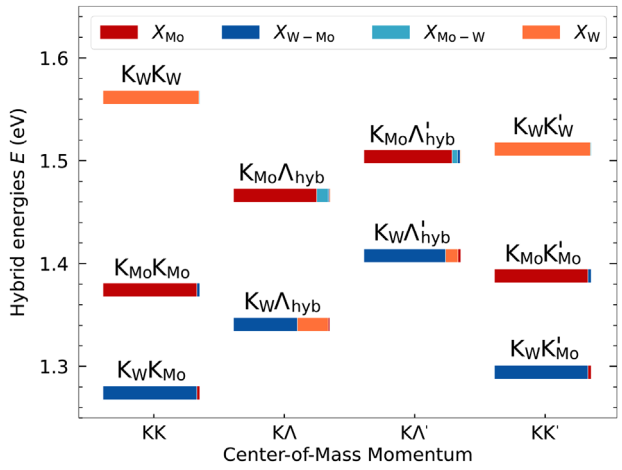

FIGURE 2 Hybrid-exciton energy landscape for $MoSe_2$-WSe_2 (R_h^h stacking). We use different colors for depicting the four initial intra- and interlayer excitonic states named with $X_{l_h-l_e}$ (using only one index for intralayer excitons). The final hybrid exciton states are denoted with two capital letters (K, Λ) describing the valley and the subscripts (W, Mo) describing the layer, in which the hole (first letter) and electron (second letter) are localized. We highlight for each hybrid exciton the percentage of the involved intra- and interlayer exciton states. Due to the strong tunneling experienced by electrons, the states in the $K\Lambda^{(\prime)}$ valleys are strongly hybridized. Note that we plot only a selection of low-energy hybrid exciton states contributing directly to the relaxation dynamics.

the corresponding hybrid-exciton energies $\mathcal{E}^{\eta}_{\mathbf{Q}}$. With the procedure described above, we have a microscopic access to the full spectrum of strongly or weakly hybridized exciton states, including bright KK as well as momentum-dark intervalley states,[36,37] such as KΛ′ and KK′, cf. Figure 2 that will be discussed further below.

Finally, we consider the interaction of hybrid exciton states with phonons. As we restrict our study to the low-density regime, exciton-exciton scattering can be neglected.[38] Starting from the electron-hole picture and performing the same change of basis as described above, we obtain the following Hamiltonian for the hybrid–exciton–phonon interaction[30]

$$H_{\text{Y-ph}} = \sum_{\substack{\mathbf{Q},\mathbf{q},\\ j,\eta,\xi}} \mathcal{D}^{\xi\eta}_{j\mathbf{q}\mathbf{Q}}\, Y^{\xi\dagger}_{\mathbf{Q}+\mathbf{q}}\, Y^{\eta}_{\mathbf{Q}}\, b_{j,\mathbf{q}} + h.c. \tag{2}$$

as well as for the hybrid–exciton–light coupling $H_{\text{Y-l}} = \sum_{\sigma,\mathbf{Q},\eta} \mathbf{A}\cdot\mathcal{M}^{\eta}_{\sigma\mathbf{Q}}\, Y^{\eta}_{\mathbf{Q}_{\parallel}} + h.c.$ All details on the basis transformation and the resulting hybrid matrix elements can be found in the Supporting Information.

Having determined the Hamilton operator $H = H_{\text{Y}} + H_{\text{Y-ph}} + H_{\text{Y-l}}$ for hybrid-excitons and their interaction with phonons and light, we can now derive equations of motion describing the exciton dynamics. Here, we exploit the Heisenberg equation of motion for the occupation numbers $N^{\eta}_{\mathbf{Q}} = \langle Y^{\eta\dagger}_{\mathbf{Q}} Y^{\eta}_{\mathbf{Q}}\rangle$, truncating the Martin–Schwinger hierarchy arising from the exciton phonon-scattering within the second-order Born–Markov approximation.[36,39–41] Considering separately the coherent polarization $P^{\eta}_{\mathbf{Q}} = \langle Y^{\eta\dagger}_{\mathbf{Q}}\rangle$ and the purely incoherent population $\delta N^{\eta}_{\mathbf{Q}} = N^{\eta}_{\mathbf{Q}} - |P^{\eta}_{\mathbf{Q}}|^2$, we arrive at the semiconductor Bloch-equations in hybrid-exciton basis

$$i\hbar\dot{P}^{\eta}_{0} = -(\mathcal{E}^{\eta}_{0} + i\Gamma^{\eta}_{0})P^{\eta}_{0} - \mathcal{M}^{\eta}_{0}\cdot\mathbf{A}(t) \tag{3}$$

$$\delta\dot{N}^{\eta}_{\mathbf{Q}} = \sum_{\xi} W^{\xi\eta}_{\mathbf{0Q}}|P^{\eta}_{0}|^2 + \sum_{\xi,\mathbf{Q}'}\left(W^{\xi\eta}_{\mathbf{Q}'\mathbf{Q}}\delta N^{\xi}_{\mathbf{Q}'} - W^{\eta\xi}_{\mathbf{QQ}'}\delta N^{\eta}_{\mathbf{Q}}\right).$$

The details on the scattering tensor $W^{\eta\xi}_{\mathbf{QQ}'}$ can be found in the Supporting Information. Equation (3) provides full microscopic access to the dynamics of hybrid excitons, including optical excitation as well as phonon-scattering-induced relaxation across intra- and intervalley as well as intra- and interlayer states, effectively giving rise to a multi-step charge transfer process.

HYBRID EXCITON LANDSCAPE

We focus here on the two most studied heterostructures in literature, MoS_2-WS_2 and $MoSe_2$-WSe_2. For simplicity, we show the results for the latter in the main text and the former in the Supporting Information. We start by presenting the hybrid exciton landscape that has been calculated by solving the Wannier equation in the hybrid-exciton basis, cf. Figure 2. This energy landscape is the key to understanding the charge transfer process. We use the following notation for the hybrid exciton states: the capital letters describe the valley and the subscript the layer, where the first letter denotes the hole and the second the electron. To give an example, $K_WK'_{Mo}$ means that the hole is located at the K point of the WSe_2 layer, while the electron is localized at the K′ valley of the $MoSe_2$ layer. Furthermore, we use the subscript hyb to underline that the electron/hole in the corresponding valley is strongly hybridized between both layers, for example, in $K_W\Lambda_{hyb}$, the electron at the Λ valley lives in both layers.

Figure 2 shows the energy landscape of hybrid-excitons in the $MoSe_2$-WSe_2 heterostructure for the case of R_h^h stacking, that is, the metal atoms of one layer are placed on top of the metal atoms of the other layer. The corresponding landscape for the other two high-symmetry stackings R_h^X and R_h^{M27} (where either the chalcogen atom X or the metal atom M of the upper layer is above the hole/void of the other layer) as well as for the MoS_2-WS_2 heterostructure can be found in the Supporting Information. We show only the hybrid exciton states that are energetically close to or lower than the intralayer K_WK_W exciton in the WSe_2 layer, since we will resonantly excite the material at this exciton energy and phonon-driven relaxation processes will distribute the excitons toward lower energies. We have checked that the contribution of higher exciton states to the relaxation dynamics and the charge transfer process, that is, due to absorption of phonons, is negligible. Note that for this particular heterostructure, ΓK excitons do not play a role for the charge transfer process, while these are crucial for the MoS_2-WS_2 heterostructure considered in the Supporting Information.

In the exciton basis, the hybridization of electronic states corresponds to a mixing of intra- and interlayer excitons. We quantify the contribution of each state to the new hybrid-exciton states by

evaluating the mixing coefficients. Here, $|c^{\eta}_{\mu}(\mathbf{Q})|^2$ can be interpreted as the percentage of the exciton state μ inside the hybrid state η. In the presence of strong tunneling, the new hybrid states are expected to be heavily influenced by different excitonic species. In contrast, a weak tunneling should result in hybrid states that are almost purely intra- or interlayer excitons. The degree of hybridization of each state is illustrated in Figure 2 by adopting a color scheme, where we highlight for each hybrid state the different exciton contributions. Here, a hybrid state of a pure intralayer or interlayer character is just red or blue, respectively. In contrast, strongly hybridized states consist of different colors. Figure 2 illustrates that hybrid states involving excitons at the Λ valley ($K_W\Lambda_{hyb}$, $K_W\Lambda'_{hyb}$) contain large contributions of several species, whereas the states at the K valley are either intra- or interlayer excitons to a very high percentage. The weak hybridization of KK excitons is well known in literature.[42,43] The electronic wave functions at the K valley are mostly composed of d orbitals localized at transition metal atoms, which are sandwiched by the selenium atoms preventing an efficient overlap of wave functions. In contrast, the electronic wave function at the Λ valley has large contributions at the selenium atoms resulting in much more efficient hybridization of $K_W\Lambda^{(\prime)}_{hyb}$ states.[30,31,42,43]

The energetically lowest states in the investigated $MoSe_2$-WSe_2 heterostructure are $K_WK^{(\prime)}_{Mo}$ excitons that are almost purely of interlayer exciton character (blue). When exciting the material resonantly to the intralayer K_WK_W state (orange), there are a number of spectrally lower-lying states that will give rise to a phonon-mediated cascade of transitions down to the energetically lowest states. Note that the scattering process between two hybrid states requires that the initial and final states live at least partially in the same layer. Therefore, we expect the strongly hybridized exciton states $K_W\Lambda^{(\prime)}_{hyb}$ to play a major role for the relaxation dynamics and the charge transfer process.

HYBRID EXCITON DYNAMICS

Now, we investigate the time- and momentum-resolved relaxation cascade of hybrid excitons after an optical excitation resonant to the purely intralayer K_WK_W exciton localized in the WSe_2 layer, cf. Figure 2. To focus on the charge transfer process and to avoid interplay effects with the exciting laser pulse, we directly initialize the system with a population in the K_WK_W state. We have also performed calculations, including the laser pulse and the interference of optical excitation and relaxation dynamics, which are presented in the Supporting Information. Note that we focus on the 1s ground state for all exciton species, as higher-energy states in the Rydberg-like series of excitons exhibit a much smaller scattering probability compared to the 1s-1s transitions.[44] This has been verified by numerically evaluating phonon-assisted scattering involving higher-energy states.

Evaluating the semiconductor Bloch equations (cf. Equation 3), we have full microscopic access to the time-, energy-, and momentum-resolved relaxation cascade of nonequilibrium excitons. Figure 3 shows the momentum-integrated exciton dynamics in $MoSe_2$-WSe_2 (in R^h_h stacking) at 77 K. We see a decrease of the initially populated intralayer

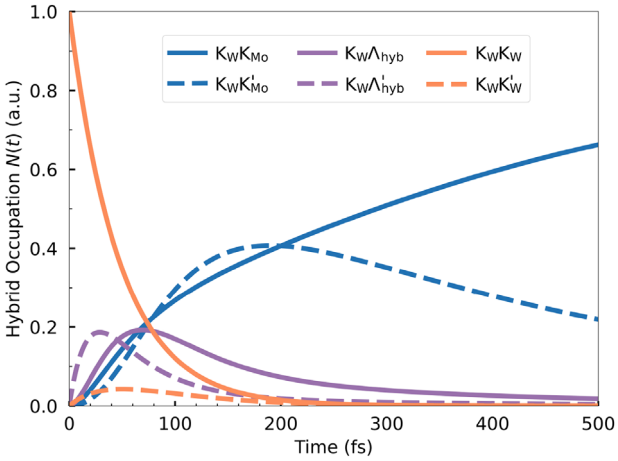

FIGURE 3 Momentum-integrated hybrid-exciton dynamics at 77 K for $MoSe_2$-WSe_2 in R^h_h stacking. By solving Equation (3), we have microscopic access to the phonon-mediated relaxation dynamics of hybrid exciton and the resulting charge transfer mechanism. Starting with an initial occupation of intralayer K_WK_W excitons localized in the WSe_2 layer (orange line) via phonon-mediated scattering into the strongly hybridized $K_W\Lambda^{(\prime)}_{hyb}$ states (purple lines), we end up in the energetically lowest interlayer $K_WK^{(\prime)}_{Mo}$ excitons (blue lines), that is, the electron has been transferred to the $MoSe_2$ layer

K_WK_W exciton state (solid orange line). At the same time, we find an ultrafast increase in the population of the hybrid $K_W\Lambda^{(\prime)}_{hyb}$ excitons on a timescale of sub-100fs (solid and dashed purple lines). The microscopic origin of this efficient scattering lies in the nature of the hybrid–exciton–phonon coupling. Phonons can only couple states that share the same layer quantum number $L = (L_e, L_h)$ as exciton-phonon scattering is considered to be a local process. For this reason, phonons can couple pure intra- and interlayer states only through scattering via hybrid states. Once the electron/hole has been scattered into a hybridized state, that is, into a superposition between both layers, there is a nonzero probability of further scattering into the opposite layer.

Following the relaxation cascade, we can track the population transfer from the hybridized $K_W\Lambda^{(\prime)}_{hyb}$ to the interlayer $K_WK^{(\prime)}_{Mo}$ excitons (solid and dashed blue lines in Figure 3). After 100 fs, the initially populated intralayer K_WK_W exciton states has been almost completely emptied and most occupation is found in the interlayer $K_WK^{(\prime)}_{Mo}$ excitons, where electrons and holes are spatially separated. As a result, the transfer of electrons from the initial WSe_2 layer into the opposite $MoSe_2$ layer occurs on sub-100fs timescale.

To further illustrate the main scattering processes governing the relaxation cascade, Figure 4 shows the momentum-resolved exciton dynamics for different times. We find that in the first step, the hybridized $K_W\Lambda_{hyb}$ and $K_W\Lambda'_{hyb}$ states are not populated (0 fs). The scattering into the latter happens on a faster timescale, as here M phonons are involved, which are known to give rise to a very efficient scattering with excitons.[45] With some delay, there is an efficient phonon-mediated scattering from these hybridized states into the interlayer K_WK_{Mo} and $K_WK'_{Mo}$ excitons. The population of the latter

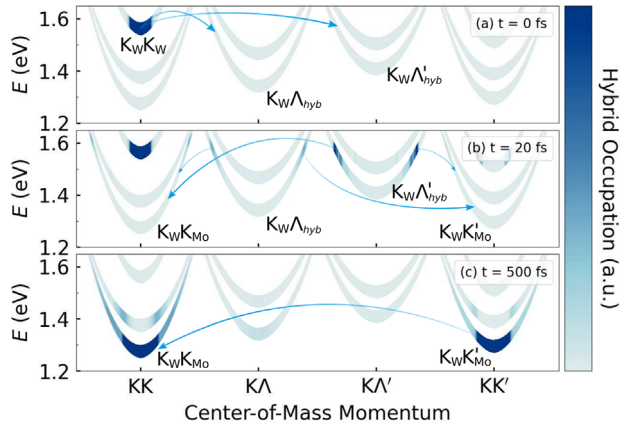

FIGURE 4 Momentum-resolved hybrid-exciton dynamics at (a) 0 fs, (b) 20 fs, and (c) 500 fs. Starting from a population created in the intralayer $K_W K_W$ exciton, we highlight the most important phonon-driven scattering processes. Note that the blue-shading in the parabolas corresponds to a microscopically calculated exciton occupation. The charge transfer of electrons occurs in a two-step process with an initial partial transfer into the hybrid $K_W\,\Lambda^{(\prime)}_{hyb}$ exciton states (with the electron living in both layers) followed by the complete transfer to the energetically lower interlayer $K_W\,K^{(\prime)}_{Mo}$ states (with the electron localized in the second layer).

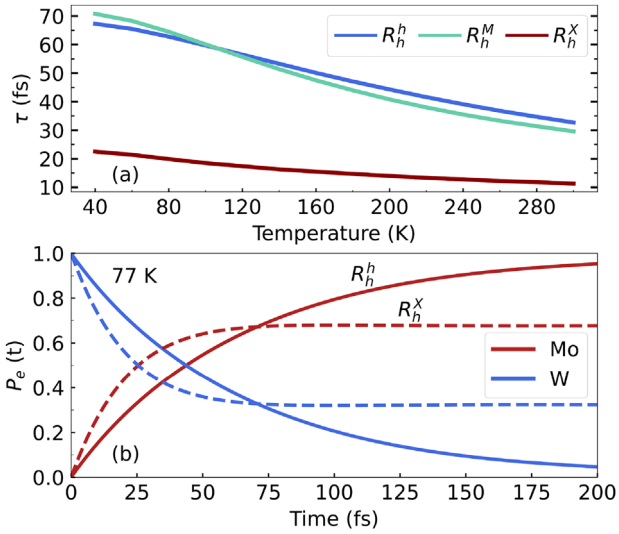

FIGURE 5 (a) Characteristic electron transfer time as a function of temperature for $MoSe_2$-WSe_2 in different high-symmetry stackings. The time is extracted from an exponential fit of the layer-dependent electron probability $P_e(t)$ as shown in part (b). We find a considerable decrease in the charge transfer time with temperature reflecting a more efficient exciton-phonon scattering. Interestingly, we predict a much faster transfer time for R^X_h stacking, as here the hybrid $\Lambda^{(\prime)}_{hyb}$ states are very close to the interlayer $K_W K^{(\prime)}_{Mo}$ states, cf the Supporting Information. The faster electron transfer speed comes at the cost of a more incomplete transfer process as the stationary occupation of the $\Lambda^{(\prime)}_{hyb}$ excitons is relatively high, where the electrons are delocalized between both layers, cf. the dashed versus solid lines in part b

occurs faster again due to the involved M phonons. In the final step, this state becomes partially depopulated in favor of the energetically lowest $K_W K_{Mo}$ state. After approximately 500 fs, a thermalized exciton distribution is reached with the highest occupation in $K_W K_{Mo}$ followed by a certain thermal occupation in $K_W K'_{Mo}$. All other states have only a negligible population.

So far, we have investigated the simplified situation of an initially populated $K_W K_W$. In a real experiment, this state will be continuously optically excited throughout a finite time window, and there will be an interplay of excitation and phonon-mediated scattering. Evaluating Equation (3), we can resolve this interplay and find the same general behavior as described above, cf. the Supporting Information. We observe the same main relaxation steps and a very similar timescale for the charge transfer mechanism. However, tracking the dynamics becomes more complicated during the initial phase of the relaxation due to the simultaneous pumping of excitons in the system that immediately start to relax very rapidly. The main difference between the simulation with a pump pulse (Figure S3) and the instantaneous initialization is that at the time when the laser pulse reaches its maximum, a large fraction of excitons has already relaxed to lower energy states, which quantitatively modifies the delay between peak populations of hybrid and interlayer exciton states. This suggests that we can capture the main features of the process using instantaneous excitation, which allows us to gain a much more intuitive picture of the charge transfer without losing generality.

INTERLAYER CHARGE TRANSFER

Summarizing the exciton dynamics in a nutshell, the initially inserted occupation of the intralayer $K_W K_W$ excitons is distributed to the energetically lowest interlayer $K_W K^{(\prime)}_{Mo}$ states through an intermediate step involving strongly hybridized $K\Lambda/\Lambda^{(\prime)}$ states. This means that the charge transfer is a two-step process, where the electron is first transferred into a hybrid state (representing a superposition of both layers) and in a second step, it is transferred to the opposite layer. The characteristic charge transfer time τ is illustrated in Figure 5a as a function of temperature for different high-symmetry stackings. We can quantify the charge transfer speed by computing the layer- and stacking-dependent probability $P_e(t) = \langle a_c^\dagger a_c \rangle$ of one electron being localized in the $MoSe_2$ layer after excitation of an intralayer state in the WSe_2 layer, cf. Figure 5b. By exponentially fitting the temporal evolution of $P_e(t)$, we can extract the characteristic electron transfer time τ. We find an ultrafast transfer rate of $\tau = 33$ fs for $MoSe_2$-WSe_2 in R^h_h stacking at room temperature. The electrons are almost completely transferred from the initially occupied WSe_2 layer to the $MoSe_2$ layer, that is, one finds the electron with a probability of 95% after 200 fs, cf. the solid red and blue lines in Figure 5b.

Since the relaxation cascade is mediated by phonons, we find a pronounced temperature dependence of the transfer time. Concretely, we predict an increase in $\tau(T)$ by approximately a factor of 2 to $\tau = 67$ fs at 40 K for R^h_h stacking. The reason is the reduced scattering efficiency with phonons at lower temperatures. Nevertheless, even at cryogenic temperatures, we find an ultrafast charge transfer as the relaxation cascade occurs toward energetically lower exciton states and is driven by phonon emission.

Interestingly, we find an unexpected acceleration of the charge transfer for R_h^X stacking (whereas, R_h^M stacking is rather similar to the R_h^h stacking investigated so far). This originates from the hybrid-energy landscape for different stackings (cf. the Supporting Information). The stronger tunneling at the KΛ valley for the R_h^X stacking[27] and the resulting larger red-shift of exciton energies has as a consequence that the relevant energy levels are closer than in other stackings, cf. Figure S2a. In particular, the strongly hybridized $K\Lambda_{hyb}$ states and the interlayer $K_W K_{Mo}^{(\prime)}$ excitons are nearly degenerate. As a result, the second step in the charge transfer process is much more efficient compared to the R_h^h stacking. Note, however, that while the charge transfer is indeed faster for the R_h^X stacking, there is only an incomplete transfer. This means that the electron is not transferred to almost 100% as in the case of R_h^h stacking, but there is still a probability of approximately 40% to find the electron in the initially populated layer, cf. the dashed lines in Figure 5b. The reason behind this is that a large percentage of the hybrid-exciton population remains in the hybrid $K\Lambda_{hyb}$ state as it is threefold degenerate and very close in energy with the lowest interlayer $K_W K_{Mo}$ state. Hence, the electron remains partially delocalized between the two layers and the charge transfer is incomplete.

So far, we have investigated the $MoSe_2$-WSe_2 heterostructure. The comparison with MoS_2-WS_2 (shown in the Supporting Information) yields the same general behavior for the hybrid-exciton relaxation dynamics. We find a somewhat slower charge transfer with $\tau = 88$ fs for R_h^h stacking at room temperature, mainly due to the much larger energy window involved in the relaxation dynamics, cf. the energy landscape in Figure S4. Analyzing the results in more detail, we find the main difference originating from the importance of $\Gamma_{hyb}K$ excitons. The strong tunneling occurring in the Γ valley results in a large red-shift of the corresponding exciton states making them energetically lowest in MoS_2-WS_2. Interestingly, we find that in contrast to $MoSe_2$-WSe_2 discussed above, we find here the slowest charge transfer for the R_h^X stacking. This can be explained by considering Γ_{hyb} K_W states, which trap excitons. The reason behind this is that despite $K\Lambda_{hyb}^{(\prime)}$ excitons being close in energy and sharing the same composition a scattering into these states requires a simultaneous electron and hole transfer and is thus a negligible higher-order process. A more detailed description of the relaxation dynamics as well as temperature- and stacking-dependent charge transfer times in the MoS_2-WS_2 heterostructure can be found in the Supporting Information.

In conclusion, we have developed a microscopic and material-specific theory allowing us to access the relaxation dynamics of hybrid excitons in van der Waals heterostructures. In particular, we identify the extremely efficient phonon-mediated relaxation via strongly hybridized $K\Lambda_{hyb}$ excitons as the crucial mechanism behind the ultrafast charge transfer process in the $MoSe_2$-WSe_2 heterostructure. We predict charge transfer times in the range of tens of femtoseconds that are strongly dependent on temperature and stacking of the layers. Our work presents an important step toward a microscopic understanding of the relaxation cascade and ultrafast charge transfer in technologically promising van der Waals heterostructures.

ACKNOWLEDGMENTS

We acknowledge the support from Deutsche Forschungsgemeinschaft (DFG) via SFB 1083 (Project B9) and the European Unions Horizon 2020 Research and Innovation Program, under Grant Agreement No. 881603 (Graphene Flagship).

CONFLICT OF INTEREST

The authors declare no conflict of interest.

AUTHOR CONTRIBUTIONS

Giuseppe Meneghini: formal analysis, investigation, software, writing - review & editing. Samuel Brem: conceptualization, supervision, writing - review & editing. Ermin Malic: conceptualization, funding acquisition, project administration, supervision, writing - review & editing.

ETHICAL STATEMENT

The authors confirm that they have followed the ethical policies of the journal.

DATA AVAILABILITY STATEMENT

The data that support the findings of this study are available from the corresponding author upon reasonable request.

PEER REVIEW

The peer review history for this article is available at https://publons.com/publon/10.1002/ntls.20220014

ORCID

Giuseppe Meneghini https://orcid.org/0000-0002-1889-2380
Samuel Brem https://orcid.org/0000-0001-8823-1302

REFERENCES

1. He K, Kumar N, Zhao L, et al. Tightly bound excitons in monolayer WSe_2. *Phys Rev Lett*. 2014;113:026803.
2. Chernikov A, Berkelbach TC, Hill HM, et al. Exciton binding energy and nonhydrogenic Rydberg series in monolayer WS_2. *Phys Rev Lett*. 2014;113:076802.
3. Wang G, Chernikov A, Glazov MM, et al. Colloquium: excitons in atomically thin transition metal dichalcogenides. *Rev Mod Phys*. 2018;90:021001.
4. Mueller T, Malic E. Exciton physics and device application of two-dimensional transition metal dichalcogenide semiconductors. *npj 2D Mater Appl*. 2018;2:1-12.
5. Rivera P, Schaibley JR, Jones AM, et al. Observation of long-lived interlayer excitons in monolayer $MoSe_2$–WSe_2 heterostructures. *Nat Commun*. 2015;6:1-6.
6. Miller B, Steinhoff A, Pano B, et al. Long-lived direct and indirect interlayer excitons in van der Waals heterostructures. *Nano Lett*. 2017;17:5229-5237.
7. Kunstmann J, Mooshammer F, Nagler P, et al. Momentum-space indirect interlayer excitons in transition-metal dichalcogenide van der Waals heterostructures. *Nat Phys*. 2018;14:801-805.
8. Jin C, Regan EC, Yan A, et al. Observation of Moiré excitons in WSe_2/WS_2 heterostructure superlattices. *Nature*. 2019;567:76-80.
9. Tran K, Moody G, Wu F, et al. Evidence for Moiré excitons in van der Waals heterostructures. *Nature*. 2019;567:71-75.

10. Seyler KL, Rivera P, Yu H, et al. Signatures of Moiré-trapped valley excitons in $MoSe_2/WSe_2$ heterobilayers. *Nature*. 2019;567:66-70.
11. Alexeev EM, Ruiz-Tijerina DA, Danovich M, et al. Resonantly hybridized excitons in Moiré superlattices in van der Waals heterostructures. *Nature*. 2019;567:81-86.
12. Ruiz-Tijerina DA, Fal'ko VI. Interlayer hybridization and Moiré superlattice minibands for electrons and excitons in heterobilayers of transition-metal dichalcogenides. *Phys Rev B*. 2019;99:125424.
13. Sigl L, Troue M, Katzer M, et al. Optical dipole orientation of interlayer excitons in MoSe 2- WSe 2 heterostacks. *Phys Rev B*. 2022;105:035417.
14. Holler J, Selig M, Kempf M, et al. Interlayer exciton valley polarization dynamics in large magnetic fields. *Phys Rev B*. 2022;105:085303.
15. Hong X, Kim J, Shi S-F, et al. Ultrafast charge transfer in atomically thin MoS2/WS2 heterostructures. *Nat Nanotechnol*. 2014;9:682-686.
16. Ceballos F, Bellus MZ, Chiu H-Y, Zhao H. Ultrafast charge separation and indirect exciton formation in a MoS2–MoSe2 van der Waals heterostructure. *ACS Nano*. 2014;8:12717-12724.
17. Ji Z, Hong H, Zhang J, et al. Robust stacking-independent ultrafast charge transfer in MoS2/WS2 bilayers. *ACS Nano*. 2017;11:12020-12026.
18. Merkl P, Mooshammer F, Steinleitner P, et al. Ultrafast transition between exciton phases in van der Waals heterostructures. *Nat Mater*. 2019;18:691-696.
19. Schmitt D, Bange JP, Bennecke W, et al. Formation of Moire interlayer excitons in space and time. *arXiv preprint arXiv:2112.05011*. 2021.
20. Deilmann T, Thygesen KS. Interlayer excitons with large optical amplitudes in layered van der Waals materials. *Nano Lett*. 2018;18:2984.
21. Hill HM, Rigosi AF, Rim KT, Flynn GW, Heinz TF. Band alignment in MoS2/WS2 transition metal dichalcogenide heterostructures probed by scanning tunneling microscopy and spectroscopy. *Nano Lett*. 2016;16:4831-4837.
22. Özcelik VO, Azadani JG, Yang Ce, Koester SJ, Low T. Band alignment of two-dimensional semiconductors for designing heterostructures with momentum space matching. *Phys Rev B*. 2016;94:035125.
23. Ovesen S, Brem S, Linderälv C, et al. Interlayer exciton dynamics in van der Waals heterostructures. *Commun Phys*. 2019;2:1-8.
24. Wang Y, Wang Z, Yao W, Liu G-B, Yu H. Interlayer coupling in commensurate and incommensurate bilayer structures of transition-metal dichalcogenides. *Phys Rev B*. 2017;95:115429.
25. Zheng Q, Saidi WA, Xie Y, et al. Phonon-assisted ultrafast charge transfer at van der Waals heterostructure interface. *Nano Lett*. 2017;17:6435-6442.
26. Liu F, Li Q, Zhu X-Y. Direct determination of momentum-resolved electron transfer in the photoexcited van der Waals heterobilayer W S 2/Mo S 2. *Phys Rev B*. 2020;101:201405.
27. Hagel J, Brem S, Linderälv C, Erhart P, Malic E. Exciton landscape in van der Waals heterostructures. *Phys Rev Res*. 2021;3:043217.
28. Brem S, Linderalv C, Erhart P, Malic E. Tunable phases of Moiré excitons in van der Waals heterostructures. *Nano Lett*. 2020;20:8534-8540.
29. Katsch F, Selig M, Carmele A, Knorr A. Theory of exciton–exciton interactions in monolayer transition metal dichalcogenides. *Phys Status Solidi (b)*. 2018;255:1800185.
30. Brem S, Lin K-Q, Gillen R, et al. Hybridized intervalley Moiré excitons and flat bands in twisted WSe 2 bilayers. *Nanoscale*. 2020;12:11088-11094.
31. Merkl P, Mooshammer F, Brem S, et al. Twist-tailoring Coulomb correlations in van der Waals homobilayers. *Nat Commun*. 2020;11:1-7.
32. Kormányos A, Burkard G, Gmitra M, et al. k·p theory for two-dimensional transition metal dichalcogenide semiconductors. *2D Materials*. 2015;2:022001.
33. Laturia A, Put ML, Vandenberghe WG. Dielectric properties of hexagonal boron nitride and transition metal dichalcogenides: from monolayer to bulk. *npj 2D Mater Appl*. 2018;2:1-7.
34. Song Y, Dery H. Transport theory of monolayer transition-metal dichalcogenides through symmetry. *Phys Rev Lett*. 2013;111:026601.
35. Glazov MM, Amand T, Marie X, Lagarde D, Bouet L, Urbaszek B. Exciton fine structure and spin decoherence in monolayers of transition metal dichalcogenides. *Phys Rev B*. 2014;89:201302.
36. Selig M, Berghäuser G, Richter M, Bratschitsch R, Knorr A, Malic E. Dark and bright exciton formation, thermalization, and photoluminescence in monolayer transition metal dichalcogenides. *2D Materials*. 2018;5:035017.
37. Deilmann T, Thygesen KS. Finite-momentum exciton landscape in mono- and bilayer transition metal dichalcogenides. *2D Materials*. 2019;6:035003.
38. Erkensten D, Brem S, Wagner K, et al. Dark exciton–exciton annihilation in monolayer transition-metal dichalcogenides. *Phys Rev B*. 2021;104:L241406.
39. Haug H, Koch SW. *Quantum Theory of the Optical and Electronic Properties of Semiconductors*. World Scientific Publishing Company; 2009.
40. Thränhardt A, Kuckenburg S, Knorr A, Meier T, Koch SW. Quantum theory of phonon-assisted exciton formation and luminescence in semiconductor quantum wells. *Phys Rev B*. 2000;62:2706.
41. Brem S, Selig M, Berghaeuser G, Malic E. Exciton relaxation cascade in two-dimensional transition metal dichalcogenides. *Sci Rep*. 2018;8:1-8.
42. Cappelluti E, Roldán R, Silva-Guillén JA, Ordejón P, Guinea F. Tight-binding model and direct-gap/indirect-gap transition in single-layer and multilayer MoS 2. *Phys Rev B*. 2013;88:075409.
43. Gillen R, Maultzsch J. Interlayer excitons in $MoSe_2/WSe_2$ heterostructures from first principles. *Phys Rev B*. 2018;97:165306.
44. Brem S, Zipfel J, Selig M, et al. Intrinsic lifetime of higher excitonic states in tungsten diselenide monolayers. *Nanoscale*. 2019;11:12381-12387.
45. Jin Z, Li X, Mullen TJ, Kim WK. Intrinsic transport properties of electrons and holes in monolayer transition-metal dichalcogenides. *Phys Rev B*. 2014;90:045422.

SUPPORTING INFORMATION

Additional supporting information can be found online in the Supporting Information section at the end of this article.

How to cite this article: Meneghini G, Brem S, Malic E. Ultrafast phonon-driven charge transfer in van der Waals heterostructures. *Nat Sci*. 2022;2:e20220014. https://doi.org/10.1002/ntls.20220014